Chorus Waves in Geospace and their Influence on Radiation Belt Dynamics

Jacob Bortnik, Richard M. Thorne, Wen Li, and Xin Tao

| 8.1 Introduction | 193 |
|---|-----|
| 8.2 Characteristics of chorus waves | 194 |
| 8.3 Introduction to resonant wave particle interactions | 197 |
| 8.4 Modes of interaction | 201 |
| 8.5 Summary and conclusions | 212 |
| References | 212 |

■ Abstract

This chapter explores the physics of the resonant interactions between whistler-mode chorus waves and energetic electrons, typical of the near-Earth space environment, and focuses specifically on those elements of the resonant interaction that are unique to chorus. After describing the general morphology and characteristics of chorus waves, we introduce the basic elements of the resonant wave-particle interaction by examining the regions of resonance, and trajectories of resonant electrons in velocity space. We then turn our attention to the different modes of scattering that resonant electrons can experience in response to chorus waves. First, the linear response is discussed and it is shown how multiple linear wave-particle interactions can cause diffusive spreading of the electron population. An example is given of a recent ultrarelativistic acceleration event that has been successfully modeled using a quasilinear diffusion approach. We then discuss the regimes of nonlinear phase bunching and phase trapping and show how these effects manifest under progressively more realistic conditions: first by including large amplitude waves, then subpacket structure, frequency drift, and finally a realistically modeled chorus element based on satellite observations. Throughout the chapter, particular emphasis is placed on developing a conceptual, intuitive understanding of the ideas presented, for

the worker who may be new to this field. We conclude by briefly outlining a few of the open areas where understanding is still incomplete, and which are ripe for discoveries in the coming years.

8.1 Introduction

The resonant interaction of energetic electrons with whistler-mode chorus waves has become a topic of extreme interest in recent years, mainly due to two reasons: the first is the steadily developing realization that chorus plays a key role in rebuilding radiation belt fluxes to very high levels after they have been depleted, by accelerating lower energy electrons (~100 keV) to relativistic energies on timescales that are comparable to a day [e.g., Horne et al., 2005; Thorne et al., 2013]. A second, and closely related reason, is the recent launch of the twin Van Allen Probes on August 30, 2012 [Mauk et al., 2012] whose primary objectives involve the understanding of the physical processes responsible for radiation belt dynamics, where chorus is thought to play a fundamental role [Thorne, 2010]. In addition to the electron radiation belt population, recent studies have demonstrated that chorus is the dominant driver of the pulsating aurora [Nishimura et al., 2010, 2011; Li et al., 2012] and the diffuse aurora [Thorne et al., 2010; Ni et al., 2011; Tao et al., 2011a], which involve the precipitation of electrons into the Earth's dense upper atmosphere, with energies of tens of keV, and a few keV, respectively. The diffuse aurora, in particular, acts as an essential feedback element in the coupled magnetosphere-ionosphere system, by modifying ionospheric conductivities, and hence 'shorting out' the electric field in regions of the ionosphere, which, when mapped out to the magnetosphere along magnetic field lines, tends to slow the rate of convection and transport. Thus, whistler-mode chorus waves form a key component of the dynamic and highly coupled inner magnetospheric environment, by transferring energy from the lower energy plasma sheet electron population to the high energy radiation belt population, by scattering and precipitating the lower energy electrons into the atmosphere and creating auroras, and by modifying the ionospheric conductivities and hence the macroscopic structure of the convection electric field that drives geomagnetic activity.

In this chapter, we aim to introduce and explore the resonant interaction of energetic electrons with whistler-mode chorus waves, and focus specifically on the unique aspects of chorus waves that give rise to these interactions. Chorus waves occur in a specific frequency band, at well-defined regions of geospace, and with unique wave normal and Poynting vector characteristics, which limit the morphology of the interaction to specific regions in velocity space. These chorus characteristics are described in Section 8.2 and the basic trajectories of resonant particles in velocity space are introduced and discussed in Section 8.3. Unlike the conceptual framework of quasilinear diffusion which assumes a band of small amplitude, uncorrelated waves, chorus occurs with widely varying amplitudes which can lead to qualitatively different responses of the resonantly interacting electrons. These different responses are discussed in Section 8.4, where simply increasing the amplitude of the wave results in scattering that progresses from linear, to phase

bunched, to phase trapped. Section 8.4.1 discusses the linear response, and shows how it evolves from individual wave-particle interactions, and how it has been applied to ultra-relativistic electron acceleration. Section 8.4.2 then shows those aspects of the chorus wave-electron interaction that are not described by quasilinear theory, namely the finite (i.e., large) amplitude of the chorus wave leading to nonlinear phase bunching and trapping, the modulation of the chorus wave amplitude, how it can be modeled and understood in a simplified way, and finally a realistic chorus element with all its unique features, such as frequency variation, amplitude modulation, and propagation effects.

8.2 Characteristics of chorus waves

Whistler-mode chorus waves are electromagnetic electron cyclotron (i.e., whistler mode) waves, which are naturally excited near the Earth's geomagnetic equator due to cyclotron resonant interactions with anisotropic, plasma sheet electrons in the energy range of ~1–100 keV [e.g., Kennel and Petschek, 1966; Nunn, 1974; Nunn et al., 1997; Omura et al., 2008, 2009] that are injected into the inner magnetosphere during geomagnetically active conditions [e.g., Burtis and Helliwell, 1969; Tsurutani and Smith, 1977; Li et al., 2009; Meredith et al., 2003].

Figure 8.1a shows a cutaway view of the inner magnetosphere, where the drift of plasma sheet electrons from the magnetotail, through the dawn side, and into the day side of the Earth is illustrated using a red arrow. As these plasma sheet electrons drift closer to the Earth from the nightside, their anisotropy is increased due to the conservation of the first two adiabatic invariants [Roederer, 1970], leading to a source of free energy which is then released in the form of chorus waves. Consequently, chorus waves are predominantly observed over the Magnetic Local Time (MLT) range of \sim 2100–1500, coincident with the drift trajectories of plasma sheet electrons. However, the latitudinal extent to which chorus waves propagate is controlled by a more subtle effect.

A unique feature of chorus waves is the observation that they only propagate away from the geomagnetic equator [Lauben et al., 1998, 2002; Ledocq et al., 1998; Santolik et al., 2010; Li et al., 2013a], implying that their source region is located at, or very near to the equator [e.g., Helliwell, 1967; Nunn, 1974; Trakhtengerts, 1999; Omura et al., 2008, 2009]. Second, some mechanism extinguishes the wave energy in the course of their propagation, before the waves are able to reflect at high latitudes and return to the equator. The first implication follows directly from the source of free energy that creates the waves, namely the temperature anisotropy of the electron populations which is maximum at the equator (i.e., the region of minimum B along the field line, where $\sim 90^{\circ}$ electrons are trapped). The second implication, namely the necessity of a damping mechanism, is less obvious since the plasma is generally collisionless, and thus requires some sort of wave-particle interaction to play the role of collisions and remove the energy from the wave. An illustration of the chorus wave excitation at the

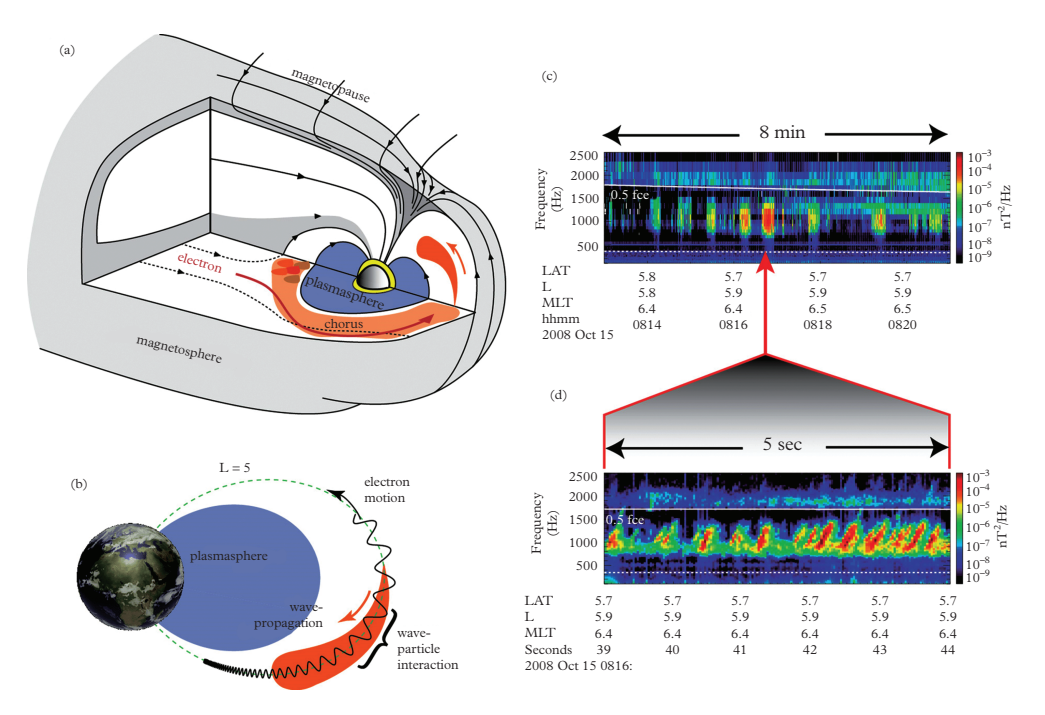


Figure 8.1 Morphology of chorus waves in the Earth's inner magnetosphere. (a) A cutaway of the magnetosphere showing the drift of plasma sheet electrons from the magnetotail, through the dawn side and into the dayside. The equatorial projection of the chorus source region is shown in orange as well as a meridional projection of chorus propagation on the dayside. (b) A meridional projection illustrating the propagation of chorus waves from the equatorial region toward the southern hemisphere, and the traversal of an energetic electron through the chorus wave field. (c) An 8-minute observation of chorus waves from the THEMIS satellite, showing the large scale (~minute) modulation of the wave intensity. (d) A 5-second expanded view of a sequence of rising-tone chorus elements from (c). The white line represents half of the equatorial electron gyrofrequency.

geomagnetic equator, propagation to high latitudes, and interaction with an energetic electron is given in Figure 8.1b where the orange color denotes the chorus wave packet. In a study that combined ray tracing with path-integrated linear growth rates calculated using statistical data from the CRRES satellite, Bortnik et al. [2007] showed that Landau resonant interactions of chorus with ~1 keV electrons resulted in damping rates that produced latitudinal propagation characteristics that were remarkably consistent with chorus observations, and that varied as a function of wave frequency, L-shell, and MLT. Nightside chorus was seen to propagate to latitudes of ~10°–15° which steadily increased with increasing MLT to latitudes of ~25°–30° (or more) on the dayside, consistent with observations of the chorus distribution. The modeled wave normal angle distribution of chorus power as a function of latitude was shown to be relatively field aligned [Chen et al., 2013], with most of the power contained within ~20°–30°, since

Landau interactions quickly damp more oblique wave normal angles, and is consistent with observations [Agapitov et al., 2013; Santolik et al., 2014]. Nightside chorus is very intense [Li et al., 2009] and more directly controlled by geomagnetic activity [e.g., Tsurutani and Smith, 1974, 1977] than dayside chorus which is relatively weak and does not seem to be strongly modulated by substorm activity. These observations are consistent with convective injection on the nightside, which brings large fluxes of ~10-100 keV electrons into the inner magnetosphere which then excite intense nightside chorus waves. The convective injection also brings large fluxes of electrons in the suprathermal range (~1 keV) which quickly damp oblique chorus waves and prevent them from traveling further than $\sim 10^{\circ}-15^{\circ}$ in latitude away from the equator. As these injected electrons drift around dawn to the dayside, their fluxes diminish due to waveparticle scattering and precipitation into the atmosphere to cause the diffuse aurora. This scattering is energy dependent, such that ~keV electrons are depleted faster than the $\sim 10-100$ keV electrons, and the damping rates are consequently reduced on the dayside, allowing the waves to propagate further away from the equator along the field line. In addition, drift shell splitting due to the Earth's compressed, asymmetric magnetic field leads to an enhancement of the anisotropy of the \sim 10–100 keV electron population on the day side [e.g., Li et al., 2010], and hence ensures that sufficient free energy is available for the excitation of chorus waves. Studies have also demonstrated that there is a region on the dayside where the compressed magnetic field lines tend to remain uniform over extended distances, dubbed the 'dayside uniform zone' where chorus can be readily excited [Keika et al., 2012], and since Landau resonant electron fluxes are reduced, chorus waves propagate to high latitudes with little damping. Since there is a few hour time-lag between the electron injection on the nightside and the excitation of the chorus on the dayside (which is also largely controlled by magnetic-gradient induced anisotropy), the correlation of chorus to geomagnetic activity is much weaker than on the nightside.

The latitudinal distribution of the chorus wave power is thus largely shaped and controlled by the distribution of the \sim keV suprathermal fluxes relative to the \sim 10–100 keV source population of electrons. The resulting latitudinal distribution, in turn, has profound implications on the net balance between chorus-driven loss and acceleration of radiation belt particles, since equatorially confined chorus waves tend to resonate with higher pitch-angle electrons, whereas chorus waves at high latitudes can more readily access the loss-cone [e.g., Horne and Thorne, 2003]. For a given electron energy, the net effect of the chorus waves on the particle population is critically dependent on the distribution of chorus wave power as function of latitude, and thus indirectly, on the \sim keV electron population that controls this distribution.

In addition to the global distribution of chorus wave power as a function of L, MLT, latitude, and time (where time is taken as, for example, storm or substorm phase), chorus shows a remarkable degree of structure over a wide range of temporal and spatial scales. Figure 8.1c shows an 8-minute observation of chorus waves recorded on the Time History of Events and Macroscale Interactions during Substorms (THEMIS) E satellite on Oct 15, 2008, which reveals a periodic pulsation on the scale of $\sim 10-100$ s, which has been shown to be directly related to the pulsating aurora observed by ground-based all

sky imagers [e.g., Nishimura et al., 2010, 2011]. When expanded further, as in Figure 8.1d over a 5 s timescale, the 'on' phase of the periodic pulsation is seen to consist of a multitude of distinct rising tones, with time scales on the order of ~ 0.1 s and separation on the order of $\sim 0.5-1$ s. It is these chorus elements that, when played over a loud speaker, resemble the sound of a rookery of birds in their 'dawn chorus' and give rise to the name of the emission [Storey, 1953; Isted and Millington, 1953]. When expanded further still (not shown) it is found that each individual chorus element consists of a sequence of finely structured sub-elements, with duration on the order of a few milliseconds [e.g., Santolík et al., 2004]. These temporal structures have also been shown to have corresponding spatial scales, for example the $\sim 10-100$ s periodic pulsation of the chorus shown in Figure 8.1c has been associated with regions of scale length \sim 1 Re [Nishimura et al., 2011] that pulsate coherently and seem to be associated with density enhancements and depletions [Li et al., 2011]. These regions are illustrated schematically on the nightside of Figure 8.1a and have the property that each patch pulsates with a unique pattern that is uncorrelated to any of its neighboring patches thus allowing a one-to-one correlation with a patch pulsating in the ionosphere [e.g., Nishimura et al., 2010, 2011]. The individual chorus elements shown in Figure 8.1d have spatial scales that are on the order of a wavelength (tens of km) in the direction perpendicular to the magnetic field line and roughly a factor of 10 larger in the parallel direction [Santolík and Gurnett, 2003].

At the present time, the distinctive spatial and temporal scales exhibited by chorus emissions are not well understood, although they are undoubtedly associated with the physics of the generation mechanism, and much progress has been made in recent years in replicating the chorus element structure in large-scale Particle-In-Cell computer simulations [Katoh and Omura, 2006, 2007, 2011; Omura et al., 2008, 2009; Hikishima et al., 2010; Omura and Nunn, 2011; Hikishima and Omura, 2012]. However, it is relatively straightforward to assess the effect that such structuring has on the electron scattering, as shown later in this chapter. To begin, we describe the essential elements of the wave-particle interaction process in the next section.

8.3 Introduction to resonant wave particle interactions

A charged particle moving in a background magnetic field $\mathbf{B}_0 = \mathbf{z}B_0$ will gyrate in the direction perpendicular to \mathbf{z} with an angular frequency $\Omega = -qB_0/m$ where q, B_0 , and m are the particle's (signed) charge, magnetic field magnitude, and non-relativistic mass, respectively. If we neglect the small radiative loss due to the particle's constant centripetal acceleration, it can be said that the particle will remain in the same trajectory forever without any alteration of its total energy E or equatorial pitch angle $\alpha_0 = \tan^{-1}(v_\perp/v_\parallel)$ (here, v_\perp and v_\parallel are the components of the particle velocity perpendicular and parallel to \mathbf{B}_0 , respectively). However, if a circularly polarized wave with angular frequency ω and wave number k is allowed to propagate along the field line and the charged particle moves through this wave, the situation changes considerably and the particle is able to respond to the electromagnetic wave field in a number of ways. For purposes of discussion, we

shall assume that the wave has electric and magnetic field components denoted by $E_{\rm w}$ and $B_{\rm w}$, respectively, and further that the particle dynamics are primarily governed by the background magnetic field, so that the wave field constitutes only a small perturbation, i.e., $B_{\rm w}/B_0 \ll 1$. It might be intuitively expected that the wave field will generally appear to the particle as a minor perturbative noise whose effects will average to zero over several gyroperiods. However, if the particle moves through the wave packet with a particular parallel velocity such that the Doppler-shifted wave frequency $\omega + kv_{||}$ is exactly equal to the gyrofrequency of the particle Ω/γ (where $\gamma^2 = 1/(1-v^2/c^2)$ is the relativistic correction factor), then the particle will experience the wave field as a quasi-stationary electromagnetic structure in its frame of reference, and may begin to deviate significantly from its unperturbed trajectory. This is the basis of a resonant wave-particle interaction.

The equation describing the wave-particle interaction process is the Lorentz force equation, which can be expressed as:

$$\frac{d\mathbf{p}}{dt} = q \left(\mathbf{E}_{\mathbf{w}} + \frac{\mathbf{p}}{m\gamma} + \left[\mathbf{B}_{0}(\lambda) + \mathbf{B}_{\mathbf{w}} \right] \right)$$
(8.1)

where $\mathbf{p} = \gamma mv$ is the particle momentum, and the magnetic field has been explicitly split into the wave component $B_{\rm w}$ and background field B_0 , which varies as a function of latitude λ . Equation (8.1) is a vector equation consisting of 3 component equations in x, y, z, that can be readily transformed to a more convenient coordinate system with components parallel and perpendicular to the field line, and an angle η that represents phase angle between v_{\perp} and $B_{\rm w}$. For purposes of illustration, we assume that the wave is propagating strictly along the field line, and that the particle is non-relativistic, so that after gyro-averaging and neglecting second order terms, the equations result in the coupled set of ordinary differential equations:

$$\begin{split} \frac{\mathrm{d}v_{\parallel}}{\mathrm{d}t} &= \left(\frac{qB_{w}}{m}\right)v_{\perp}\sin\eta = \frac{v_{\perp}^{2}}{2B}\frac{\partial B}{\partial z} \\ \frac{\mathrm{d}v_{\perp}}{\mathrm{d}t} &= -\left(\frac{qB_{w}}{m}\right)\left(v_{\parallel} + \frac{\omega}{k}\right)v_{\perp}\sin\eta + \frac{v_{\perp}v_{\parallel}}{2B}\frac{\partial B}{\partial z} \\ \frac{\mathrm{d}\eta}{\mathrm{d}t} &= \Omega - \omega - kv_{\parallel} \end{split} \tag{8.2}$$

The set of equations (8.2) has been used extensively in past studies of wave-particle interactions [Dysthe, 1971; Inan et al., 1978; Bortnik et al., 2008] and only a few key features will be highlighted here. The first point to note is that if we set $B_{\rm w}=0$ then the equations reduce to purely adiabatic motion, and the particle simply travels periodically up and down a given magnetic field line, reflecting at the mirror points. In that case, the particle motion is fully described by the usual conservation of the adiabatic invariants [e.g., Roederer, 1970; Walt, 1994] and it is not necessary to use equations (8.2). If $B_{\rm w}>0$, then the wave begins to affect the particle motion through the first term on the

RHS of the top two equations of the set (8.2). However, this wave action usually averages to zero over several gyroperiods due to the rapid variation of η (and hence $\sin \eta$), unless η remains constant over some period of time, that is, if $d\eta/dt = 0 = \Omega - \omega - kv_{||}$. This condition corresponds exactly to the resonance condition.

The resonance condition implies that any particle having a parallel velocity $v_{||} = (\Omega - \omega)/k$ will be resonant with the field-aligned wave described by the parameters (ω,k) regardless of its perpendicular velocity which would appear as a straight line when plotted in velocity-space (i.e., in the $v_{||}$ - v_{\perp} plane). If we generalize the resonance condition by including a relativistic mass correction, i.e., Ω is replaced with Ω/γ , the resonance condition becomes $\Omega/\gamma - \omega - kv_{||} = 0$, or $\omega + kv_{||} = \Omega(1 - v_{||}^2/c^2 - v_{\perp}^2/c^2)^{1/2}$, which now couples the perpendicular velocity into the resonance condition, and the formerly straight lines in velocity space which represented the resonance condition become resonant ellipses.

An example of two resonant ellipses is shown in Figure 8.2, where the parameters have now been specialized to represent chorus, with $\omega_1=0.1\Omega$ and $\omega_2=0.5\Omega$ representing the typical lower and upper frequency bounds of lower-band chorus, $\Omega=2\pi(7\text{ kHz})$ representative of the equatorial region at L \sim 5, and $n_{\rm e}=10.23\,{\rm cm}^{-3}$ giving $\omega_{\rm pe}/\Omega=4.1$. Together with the resonance curves (shown in solid) is a series of constant energy surfaces depicted using dashed lines, so that the intersection between these constant energy surfaces and the resonant ellipses indicates the resonant energies and approximate pitch angles that will be able to resonate with each of the waves. It should be noted that for positive values of the wave's phase velocity as depicted in the figure, i.e., $v_{\rm ph1}=\omega_1/k_1>0$ and $v_{\rm ph2}=\omega_2/k_2>0$, the first order cyclotron resonance will typically require that the respective resonance velocities be negative, i.e., $v_{\parallel 1}^{\rm res}<0$ and $v_{\parallel 1}^{\rm res}<0$. However, for sufficiently energetic electrons, γ can be large enough that $\Omega/\gamma=\omega$ and $v_{\parallel 1}^{\rm res}=0$, or even $v_{\parallel 1}^{\rm res}>0$ giving a relativistically shifted co-streaming interaction, or the previously described relativistic turning acceleration [e.g., Omura et al., 2007; Furuya et al., 2008].

Having determined the resonant energies involved in the wave-particle interaction, we next consider the approximate trajectory taken by the resonant particles, when they are acted upon by the wave. Reverting again to the non-relativistic limit for simplicity, and for purposes of illustration, the inhomogeneity is set to zero, representative of the equatorial region, and the set of equations (8.2) integrated once [e.g., Dysthe, 1971; Walker, 1993] to yield:

$$\left(v_{||} - \frac{\omega}{k}\right)^2 + v_{\perp}^2 = V_0^2 \tag{8.3}$$

where V_0 is a constant of integration and defines a particular trajectory for resonant particles in velocity space. It should be noted that (8.3) can be alternatively obtained by performing a Lorentzian transformation to a coordinate system which is propagating with the phase velocity of the wave. In this reference frame, the wave electric field becomes zero, and hence no energy can be exchanged between the particle and the wave,

resulting in constant radius circles in velocity space, centered on the phase velocity ω/k . The resonant particle trajectory including relativistic effects is more complicated and has been derived by Summers et al. [1998].

Returning now to Figure 8.2 where the relativistic resonant trajectories are shown as solid black curves confined between the $\omega_1 = 0.1\Omega$ and $\omega_2 = 0.5\Omega$ resonance ellipses, it is possible to visualize the energy exchange processes mediated by the chorus wave. In general, the population of electrons will be constrained to flow along the resonant trajectories shown in the figure, from regions of high phase space density to regions of low phase space density. For purposes of illustration, we have superimposed a typical phase space density onto Figure 8.2, represented by a normalized bi-Maxwellian distribution having a temperature anisotropy $A = T_L/T_{||} - 1 = 1$, and an empty loss-cone at pitch angles $\alpha < \alpha_{LC} = 3.7^{\circ}$ (typical of L = 5). There are two regions indicated in the figure, denoted by R_1 and R_2 . R_1 represents the low-energy region, where the

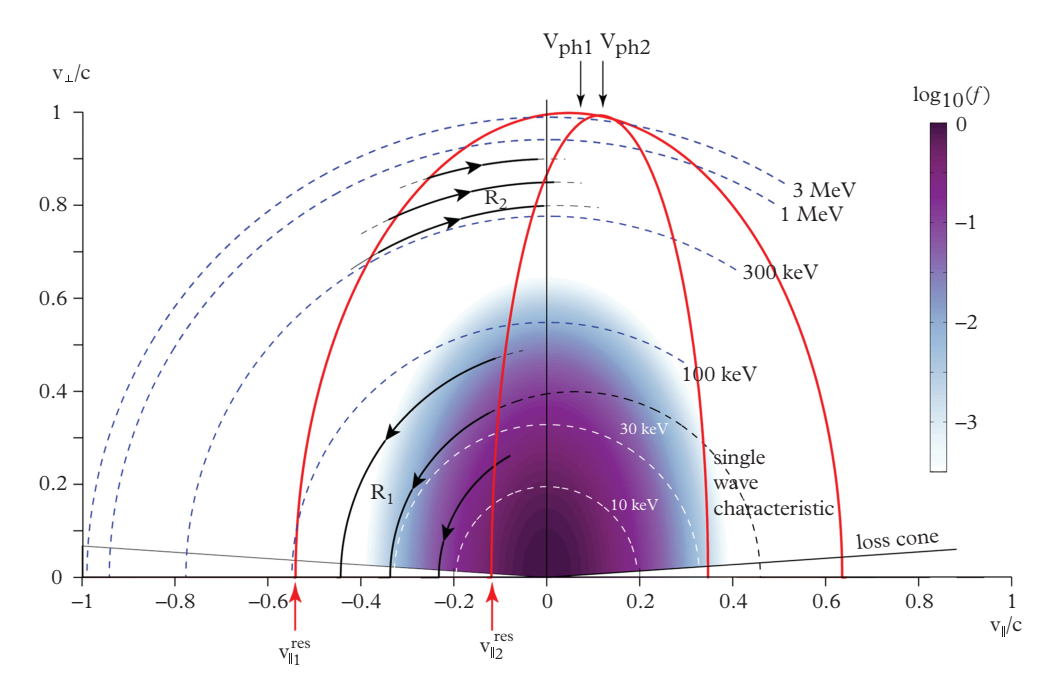


Figure 8.2 Diffusive trajectory of electrons in velocity space. The dashed lines represent surfaces of constant energy. The solid lines represent resonance ellipses corresponding to $0.1f_{ce}$ and $0.5f_{ce}$ respectively, defining the region in velocity space where particles are able to diffuse. The solid lines with arrows depict the single wave characteristics of electrons resonant with $0.1f_{ce}$ waves, where R_1 represents the region of lower energy resonant electrons, preferentially diffusing toward the loss cone, and R_2 represents the region of higher energy electrons, preferentially diffusing to higher energies. The background shading depicts a typical phase space density distribution with a mild anisotropy ($A\sim 1$) at lower energies.

combination of a temperature anisotropy and loss cone results in a PSD which is large at high pitch angles, and decreases toward low pitch angles. Thus the net flow of particles is toward low pitch angles, as indicated by the arrows. When compared to the constant energy surfaces (e.g., the 30 keV white-dashed curve), it is apparent that the resonant particles lose energy on the whole, which is transferred to the chorus wave. From the figure, it is clear that the source population of electrons that excite chorus waves in the frequency range between $\omega_1 = 0.1\Omega$ and $\omega_2 = 0.5\Omega$ lies in the range $E \sim 10$ –100 keV. The region R₂ represents the high energy electrons, and in this region the PSD decreases rapidly with increasing energy. Since the resonant trajectories increase in energy with increasing pitch angle, the lower pitch angle population will have a larger PSD and the net flow of electrons will be toward larger pitch angles. From the figure, it is apparent that electrons in the range $E \sim 300$ keV-3 MeV will absorb the wave energy and be preferentially accelerated to higher energies.

The process illustrated in Figure 8.2 depicts the essential elements of chorus-driven acceleration: the lower energy electrons (tens of keV) which contain free energy at medium to low pitch angles excite the chorus waves, and in the process get scattered toward the loss-cone and ultimately precipitated into the atmosphere, while the higher energy electrons (hundreds of keV) absorb the wave energy and get preferentially accelerated to higher pitch angles and energies. The chorus wave itself acts as a mediator of the energy flow between the different energy populations [e.g., Shklyar and Matsumoto, 2009; Thorne, 2010], and the transition energy between R₁ and R₂ occurs somewhere in the few hundred keV range [Summers et al., 2002; Horne and Thorne, 2003; Bortnik and Thorne, 2007; Turner et al., 2012].

The foregoing discussion relied on the basic assumption that electrons flow in the negative gradient direction of PSD. This is generally true but represents only one type of wave-particle interaction. Different modes of interaction are discussed next.

8.4 Modes of interaction

In order for the resonant electron population to be transported in pitch-angle and energy, the chorus wave must impart some non-adiabatic change to each electron, which can be described (in the simplest case) by the set of equations (8.2). Here, a situation is envisaged similar to Figure 8.1b, where an electron moves along its magnetic field line through the chorus wave packet, and the resonance condition, $d\eta/dt$ steadily approaches zero, at which point the particle is said to be in resonance with the wave, the wave-particle phase η (and hence $\sin \eta$) remains approximately constant over a few gyroperiods, and the first two equations of (8.2) accumulate some permanent, finite changes in v_{\perp} and v_{\parallel} (and hence also in α and E).

Intuitively, since the wave terms in equations (8.2) are proportional to $\sin \eta$, one might expect that the total scattering in α and E would be proportional to $\sin \eta$. In fact, this is

true [e.g., Inan et al., 1978], but only when the parallel velocity of the electron through the wave is adequately approximated by the unperturbed, adiabatic parallel velocity, i.e., wave-induced changes in $v_{||}$ are negligible. In those instances when $v_{||}$ is significantly perturbed from its adiabatic trajectory, in such a way as to modify the evolution of the resonance condition (final equation in (8.2)), the scattering in α and E as a function of η can be quite different from that of a sinusoid.

As an example, Figure 8.3 shows the scattering of 24 electrons, all having the same initial α and E, but being uniformly distributed in η propagating through a chorus wave packet, and experiencing a wave-particle resonance [similar to Bortnik et al., 2008]. In Figure 8.3a, the background plasma is chosen to be representative of L = 5, the wave is assumed to be field-aligned, with f = 2 kHz and $B_{\text{w}} \sim 1.4 \text{ pT}$. The particles propagate from $\lambda = -9^{\circ}$, experience a resonance at $\lambda \sim -5^{\circ}$, and emerge at $\lambda \sim -2^{\circ}$, with their pitch angles having been scattered sinusoidally as a function of the initial wave-particle phase η , as indicated in the adjoining panel on the right. Here, the scattering is small, with maximum pitch angle changes of $\sim 0.03^{\circ} - 0.04^{\circ}$.

However, if we run the same simulation, but only increase the amplitude of the wave from $B_{\rm w} \sim 1.4$ pT to $B_{\rm w} \sim 1.4$ nT, the results look completely different as shown in Figure 8.3b. One might intuitively expect from (8.2) that increasing $B_{\rm w}$ will linearly increase the range of the scattering, which is true for small values of $B_{\rm w}$, but the results of Figure 8.3b are qualitatively different, with all particles essentially behaving in a very similar way, and experiencing a rapid decrease of $\sim 5^{\circ}$ in pitch angle and ~ 5 keV in energy (shown in the right adjacent panel). In this regime, the initially uniform wave-particle phases η have all been bunched by the wave to be roughly the same, which is why all particles respond to the wave similarly. This regime is thus referred to as phase bunching.

In Figure 8.3c, the wave-particle interaction is changed slightly: the wave amplitude is kept constant at $B_{\rm w} \sim 1.4$ nT, but the wave normal is changed to be $\sim 60^{\circ}$ and the initial α and E of the particles is modified so that they will resonate with the wave at $\lambda \sim -23^{\circ}$. These parameters are discussed by Bortnik et al. [2008] and have been chosen to closely represent the recent observations of large-amplitude chorus waves [Cattell et al., 2008; Cully et al., 2008; Li et al. 2011]. Here, a combination of behaviors is observed: a large fraction of particles are phase bunched and transported to lower α and E, while some exhibit linear (and hence more symmetrical) scattering. One particle in particular, indicated by the red trajectory, is seen to rapidly increase in α , with a concomitant increase in E (not shown) of ~ 300 keV. This particle exhibits yet a third type of response known as phase trapping, where the particle's phase (relative to the wave) is trapped by the wave potential and is essentially forced to conform to the resonant velocity of the wave, as a function of latitude. This regime is known as phase trapping [e.g., Dysthe, 1971, Inan et al., 1978; Albert, 2000; Bortnik et al., 2008].

In order to determine which of the three particle responses should be expected from a particular wave-particle interaction, we return to the simplified set of equations (8.2). If the final equation is differentiated once, the equation for $dv_{||}/dt$ substituted and the

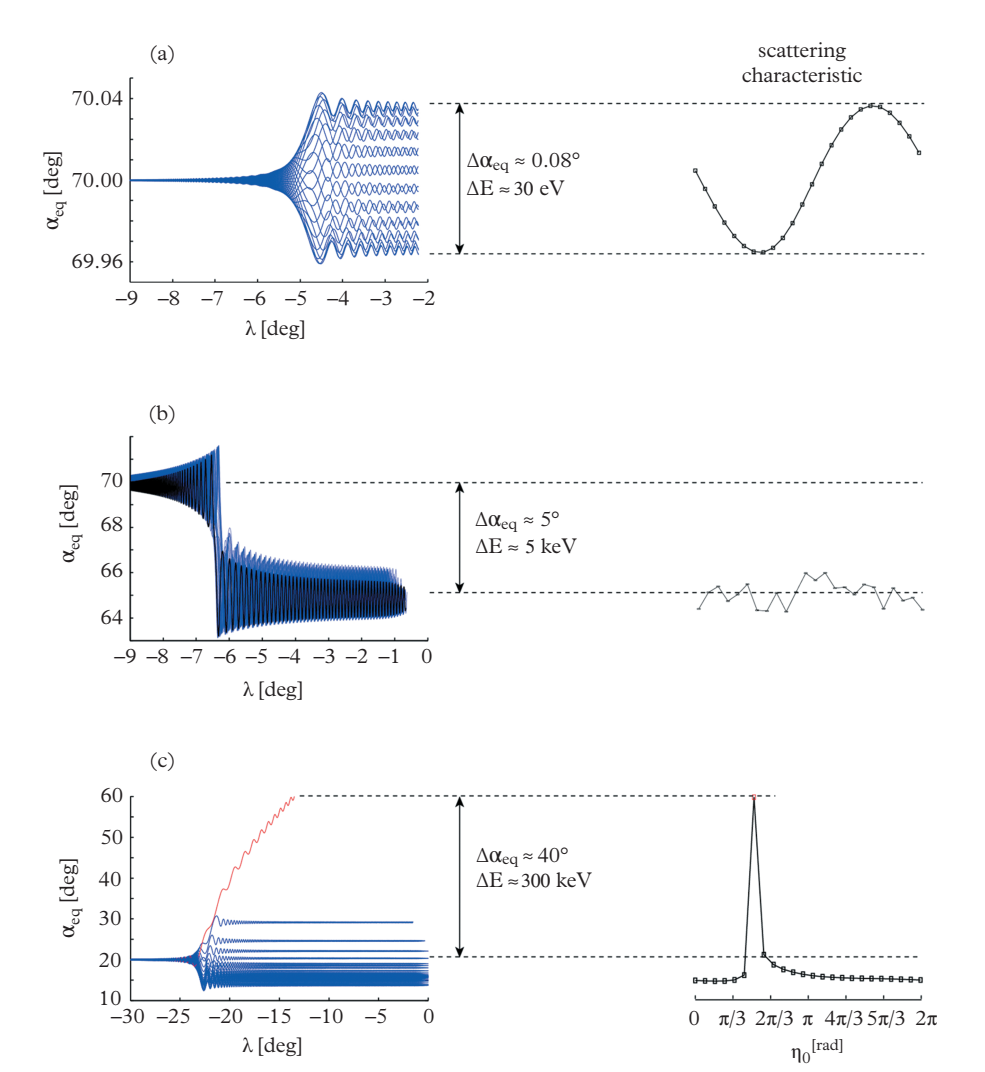


Figure 8.3 An example of three types of electron responses to a resonance with a whistler wave. (a) Low amplitude wave (~1 pT) resonating at low latitude (~5°) resulting in linear scattering , (b) a large amplitude wave (~1 nT) resonating at low latitude (~5°) resulting in phase bunching and advection, and (c) a large amplitude wave (~1 nT) resonating at high latitudes (~23°), resulting in a combination of linear scattering, phase bunching, and phase trapping (shown rising to the dotted line). The attached panels on the right represent the pitch angle scattering characteristic as a function of initial wave-particle phase angle η_0 .

small order terms neglected, the result is a second order, oscillator equation which can be written as:

$$\frac{d^2\eta}{dt^2} + k\left(\frac{qB_w}{m}\right)v_{\perp}\sin\eta = \left[\frac{3}{2} + \frac{\Omega - \omega}{2\Omega}\tan^2\alpha\right]v_{\parallel}\frac{\partial\Omega}{\partial z}$$
(8.4)

It only remains to be determined whether the 'driving' force on the RHS of the equation will dominate the 'restoring' force of the pendulum. This is done using the ratio R, which compares these two terms:

$$R = \frac{k\left(\frac{qB_w}{m}\right)v_{\perp}}{\left[\frac{3}{2} + \frac{\Omega - \omega}{2\Omega}\tan^2\alpha\right]v_{\parallel}\frac{\partial\Omega}{\partial z}} \sim \frac{B_w}{\frac{\partial\Omega}{\partial z}}$$
(8.5)

Essentially, R shows that the dynamics of the particle are determined by a competition of the wave intensity $B_{\rm w}$ against the 'mirror' force, which causes adiabatic motion, $\partial\Omega/\partial z$. When $R\ll 1$, particles will be scattered linearly, as in Figure 8.3a, whereas if $R\gg 1$, nonlinear effects will result due to the dominance of $B_{\rm w}$.

8.4.1 Quasilinear diffusion

One might legitimately ask whether the often-used quasilinear diffusion theory [Kennel and Petschek, 1966; Kennel and Engelman, 1966] can be related to the individual test particle scattering shown in Figure 8.3. To address this question in an intuitive way, we show the results of the simulation run in Figure 8.3a, but extended over the much longer interval of 60 seconds in Figure 8.4a such that a much larger number of wave-particle interactions are included (approximately 120 per particle). In contrast to the initial resonant interaction in Figure 8.3a, the trajectories of the 24 test particles are seen to spread randomly, with the average spread increasing with increasing time. Figure 8.4b shows the variance of the 24 test particles at each instant in time, displayed as a function of time, where it is now apparent that the variance increases linearly with time, which is the signature of diffusive spreading.

In fact, the comparison of test particle based diffusion and quasilinear diffusion has been done in a number of recent studies [Tao et al. 2011b, 2012] and shown to be equal. More formally, Albert [2010] has demonstrated that the analytical expressions for the quasilinear diffusion coefficients in the narrowband limit reduce precisely to the spreading derived from single-wave test particle interactions, when averaged over multiple, incoherent interactions similar to Figures 8.4a and 8.4b. Suitably averaged over a full wave distribution, the test particle based diffusion equations reproduce the quasilinear diffusion coefficients precisely.

To examine the evolution of individual test particle scattering interactions into diffusion we show the first resonant interaction again in Figure 8.4c, which is identical to Figure 8.3a but displayed as a function of time, not latitude. Since the scattering in α is sinusoidal as a function of initial η , it can be shown analytically that the results of

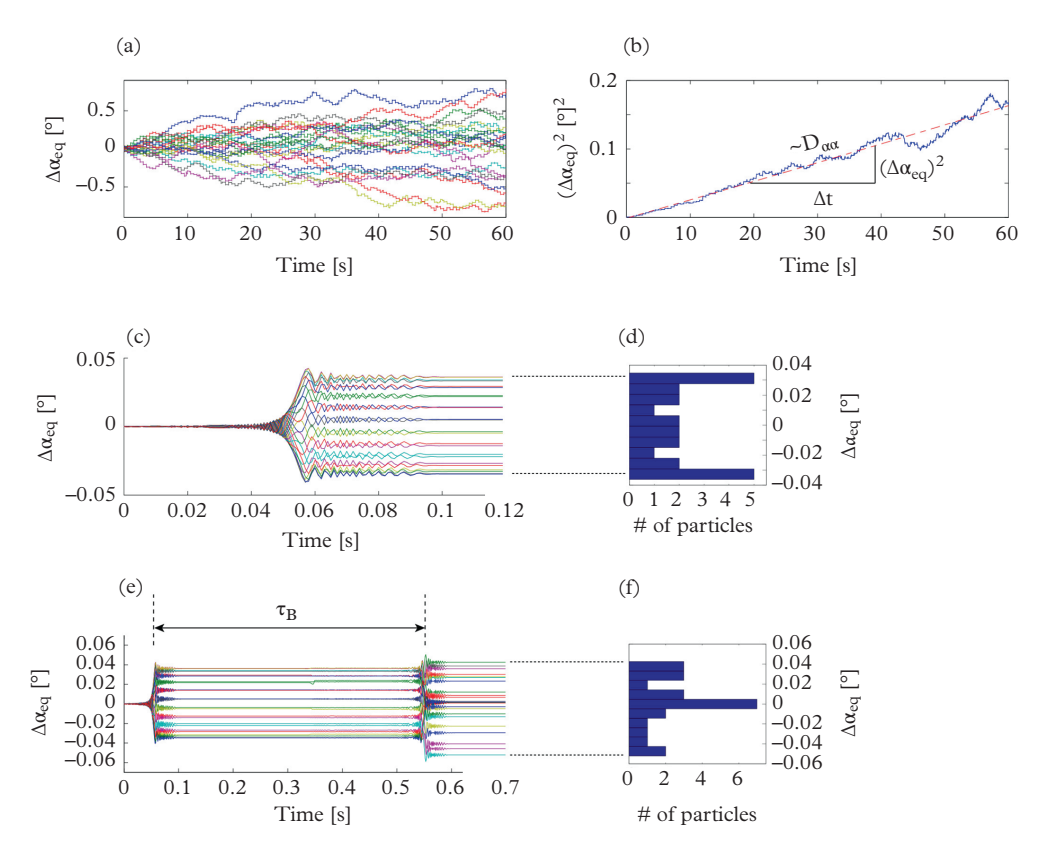


Figure 8.4 A long-run simulation of 24 electrons experiencing cumulative linear scattering interactions (similar to Figure 8.3a), resulting in quasilinear diffusive behavior. (a) Change in equatorial pitch angle of all particles as a function of time. (b) The variance of all particles, shown to be increasing linearly as a function of time, consistent with diffusive scattering. (c) An expanded view of the first 0.12 sec of the simulation, showing the first linear resonant-scattering interaction (similar to Figure 8.3a), and (d) the resultant distribution of particles at 0.12 sec. (e) An expanded view showing the first two linear resonant-scattering interactions, and (f) the resultant distribution at 0.7 sec, showing that the total scattering signature is now more normally distributed, consistent with diffusive scattering.

the first scattering take on a distribution of the form $h(\alpha) = [\pi((\Delta\alpha_{\max})^2 - (\Delta\alpha)^2)^{1/2}]^{-1}$ [Bortnik et al., 2006] where $\Delta\alpha_{\max}$ is readily determined from the equations of motion (8.2). A histogram showing the particle distribution of pitch angles following the resonant interaction is shown in Figure 8.4d, and is seen to indeed resemble $h(\alpha)$. If the time of the simulation is now extended to include the first two resonant interactions, as shown in Figure 8.4e, it is seen that the distribution of pitch angles following the second scattering no longer resembles $h(\alpha)$, but is the result of the convolution $h(\alpha)^*h(\alpha)$, leading to a more 'bell shaped' distribution. Subsequent resonant interactions each lead to a further convolution of the existing particle distribution with $h(\alpha)$ which is essentially the solution of the diffusion equation.

Having established the basic equivalence of test particle scattering with quasilinear diffusion, we can now explore the limits of applicability of quasilinear diffusion. Figure 8.5 shows an example of the results of Tao et al. [2012], where the scattering of 400 electrons has been calculated in a whistler wave packet consisting of 100 individual, incoherent components spanning the range 0.2Ω – 0.4Ω , with assumptions that satisfy those of quasilinear theory as closely as possible. Figures 8.5a and 8.5b show the pitch-angle and energy diffusion coefficients calculated using both the quasilinear theory and the test particle approach for a specific pitch angle and energy (E = 200 keV, $\alpha = 60^{\circ}$), as a function of the integrated wave intensity, $B_{\rm w}^{\rm rms}$. For low wave amplitudes, i.e., $B_{\rm w}^{\rm rms} < 300 \text{ pT}$, the diffusion coefficients agree very closely, but for large amplitudes i.e., $B_{\rm w}^{\rm rms} > 500 \text{ pT}$, the test particle based diffusion coefficients saturate, and no longer agree with the theoretical diffusion coefficients.

We define the wave amplitude at which the two approaches are different by a factor of 2 as the 'hinge' point, and plot this hinge point for seven logarithmically spaced energies between 10 keV and 1000 keV, and pitch angles between $\alpha_0 = 10^\circ$ and $\alpha_0 = 80^\circ$ in Figure 8.5c. Using L = 5 as a convenient reference point, the approximate chorus amplitudes at which quasilinear diffusion coefficients begin to saturate can be as low as 100–300 pT for electron energies with $E < \sim 100$ keV, which is the typical range of chorus wave intensities used in calculations [Meredith et al., 2003; 2012]. However, the limit of applicability increases well beyond typical, averaged observable levels for energies larger than 1 MeV, which should make diffusion simulation at ultra-relativistic energies quite accurate.

An example of the application of quasilinear diffusion to a remarkable acceleration event occurring at ultra-relativistic (i.e., several MeV) energies is shown in Figure 8.6 [Thorne et al., 2013]. Here, a sequence of observations of electrons with energies E = 2.3-7.15 MeV made during the October 8–9, 2012, geomagnetic storm with the Van Allen Probes showed a PSD increase of 3–4 orders of magnitude within a span of several hours, together with characteristic 'tophat' shaped pitch angle distributions, shown in Figures 8.6a–8.6d.

By using a newly developed technique to infer the global, time-varying chorus wave field [Li et al., 2013b], and using these chorus amplitudes to calculate diffusion coefficients that were then used to solve a Fokker–Planck diffusion equation, the theoretical phase space density distributions shown in Figures 8.6e–8.6h were obtained. The theoretical curves show remarkable consistency with observed fluxes, replicating the increase of PSD as a function of time and energy, and showing the development of the tophat distributions in pitch angle, as a function of time. These simulations are particularly significant in that they demonstrate conclusively that it is chorus waves that cause the rapid acceleration of the ultra-relativistic electrons in this event, as opposed to any of the other candidate acceleration mechanisms [e.g., Friedel et al., 2002; Thorne, 2010].

8.4.2 Nonlinear wave-particle interactions

In the previous section, we showed that when the chorus waves can be considered 'weak' (as defined by the ratio R, for example), leading to linear scattering, that the

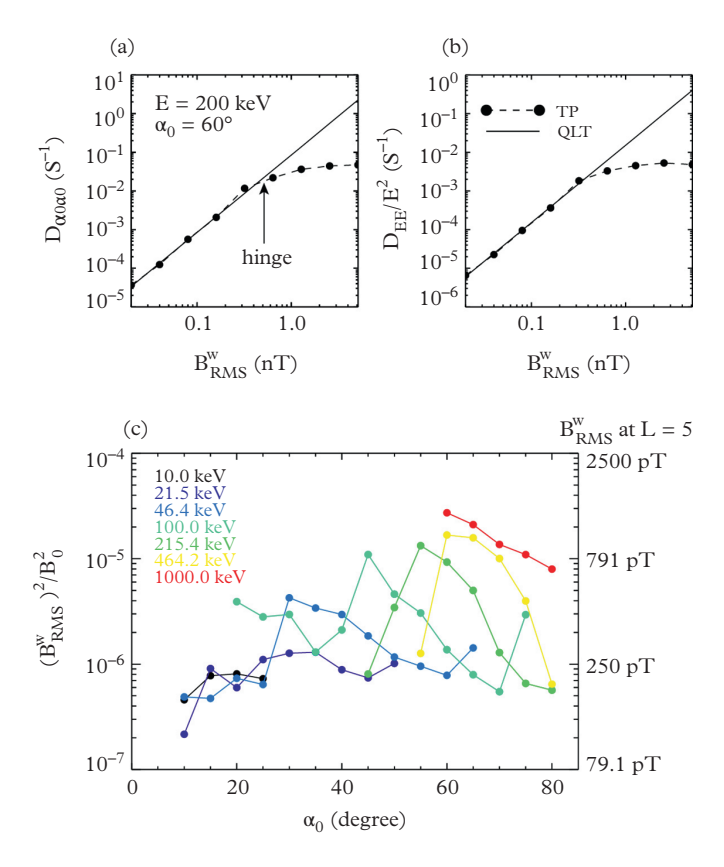


Figure 8.5 The saturation of quasilinear diffusion coefficients. (a) A comparison of the pitch-angle diffusion coefficients of 200 keV, 60° electrons calculated numerically using test particle scattering, and by quasi-linear theory, showing their agreement at low amplitudes, and deviation at large amplitudes. (b) Similar to (a) but for energy diffusion coefficients. (c) A plot of the 'hinge' points at which test particles no longer respond diffusively to wave scattering, as a function of initial pitch angle and energy. The scale on the right of the figure shows the corresponding wave amplitudes at L=5 (i.e., $B_0=250\ nT$).

result of multiple resonant interactions—even for a completely coherent monochromatic wave—reduced to the quasilinear diffusion formalism, and further that this formalism was applicable and accurate for resonant electron energies in the MeV range. However, when the waves cannot be considered 'weak', the resulting scattering can exhibit significant nonlinear behavior as shown in Figures 8.3b and 8.3c, and the result of (similar) multiple incoherent interactions is no longer diffusive but will contain strong advective

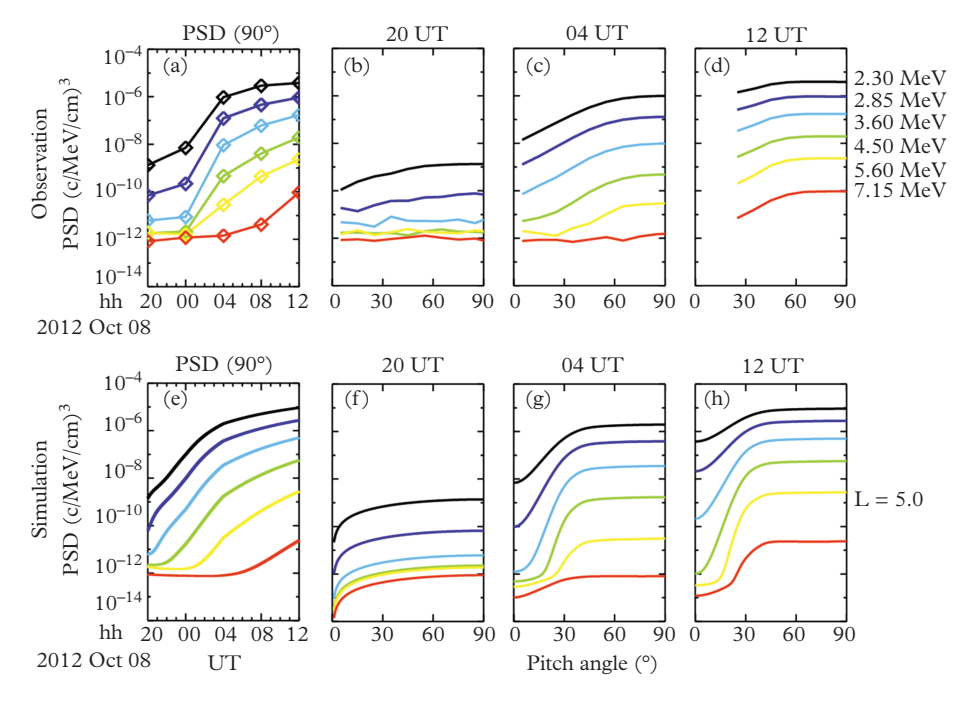


Figure 8.6 Simulation of the October 9, 2012, acceleration event of ultra-relativistic electrons. (a) Observed phase space densities on the Van Allen Probes as a function of time together with pitch angle distributions parameterized by energy at (b) October 8, 20 UT, (c) October 9, 04 UT, (d) October 9, 12 UT. Simulated results showing the progression of the phase space densities and pitch angle distributions in (e)–(h), similar to the observations in (a)–(d).

terms. In this section, we discuss such nonlinear behavior and describe how it can be understood and modeled.

The nonlinear scattering of test particles due to a single, coherent, monochromatic wave was shown in Figure 8.3 and discussed in Section 8.4.1. But realistic chorus elements contain more complexity than this simple picture, for example, consisting of a steadily rising frequency, and containing amplitude modulation within a single chorus element, which was briefly discussed in Section 8.2.

In order to quantify the effects of the chorus wave's amplitude modulation, we model the wave packet as a superposition of two sinusoids with closely spaced frequencies $\cos(\omega_1 t)$ and $\cos(\omega_2 t)$, such that the resultant wave is described by the standard formula:

$$g(t) = 2\cos\left(\frac{\omega_1 - \omega_2}{2}t\right)\cos\left(\frac{\omega_1 + \omega_2}{2}t\right) \tag{8.6}$$

Here, the small difference in frequencies $\delta \omega = (\omega_1 - \omega_2)/2$ can be interpreted as a slow modulation of a rapidly oscillating wave with frequency $<\omega>=(\omega_1+\omega_2)/2$. While

this model clearly does not capture all the intricacies of the chorus element, it is nevertheless extremely useful because it represents the amplitude modulated chorus wave in a way that can be analytically understood and analyzed [Zaslavsky, 1985, p.133]. Each component wave frequency will have its own resonant island [Lichtenberg and Lieberman, 1983], with a half-width given by:

$$\frac{\Delta p_{||}}{mc} = 2\sqrt{\frac{p_{\perp}}{mc} \frac{|\Omega|}{\omega} \frac{B_{y}^{w}}{B_{0}} \frac{1}{n}}$$

where the field is assumed to be uniform for simplicity, and the refractive index $n \gg 1$. Using the non-relativistic resonance condition, the separation between the centers of the resonant islands can be written as:

$$\frac{\delta p_{||}}{mc} = \frac{1}{c} \left| \frac{\omega_1 + \Omega}{k_1} - \frac{\omega_2 + \Omega}{k_2} \right|$$

In order to infer what the response of the particles would be to the superposed waves, it is useful to determine whether the resonant islands of the two waves overlap by comparing the width of the islands to the separation between their midpoints as shown in Figure 8.7c. This is accomplished with the overlap parameter K, defined as $K = (\Delta p_{||1} + \Delta p_{||2})/\delta p_{||}$, which is $\ll 1$ when the resonant islands are far apart and do not overlap, and >1 when resonant islands overlap and interfere with each other's trapping dynamics.

Figure 8.7 shows the results of a simulation that demonstrates the effects of varying the modulation frequency of the wave, or alternatively stated, the period between subelements defined as $\delta \tau = 1/\delta \omega$ following the work of Tao et al. [2013]. Here, the trajectories of 400 test particle electrons were calculated through a superposition of two cosine waves with a varying frequency of separation, indicated on the abscissa by δf . For low values of δf , between ~ 1 and 7 mHz, the resonant islands overlap to a great degree as shown schematically in Figure 8.7a, corresponding to a very slow modulation (large value of $\delta\tau$) and behavior that closely resembles that of a single wave, exhibiting trapping and bunching behavior as in Figure 8.3c. As δf is increased further, the resonant islands separate further and the electron scattering becomes more stochastic, illustrated in Figure 8.7b. Finally, when δf is separated further still, K > 1, and the resonant islands no longer overlap, resulting in a response which is better described by two independent, non-interfering waves that act on the particles, illustrated in Figure 8.7c. Also shown in Figure 8.7d is a probability distribution of subelement separations, scaled from Figure 5 of Santolík et al. [2004], which shows that the most frequent values of δf are in the range of $K \sim 1$, bordering between the response of two separate waves and two overlapping resonant islands which result in stochastic scattering. We note for completeness that Figures 8.7a–8.7c only serve to illustrate the topology of the resonance schematically, but additional complexity develops when particles are allowed to propagate through the phase portrait, as shown in Lichtenberg and Lieberman [1983, pp. 252-256].

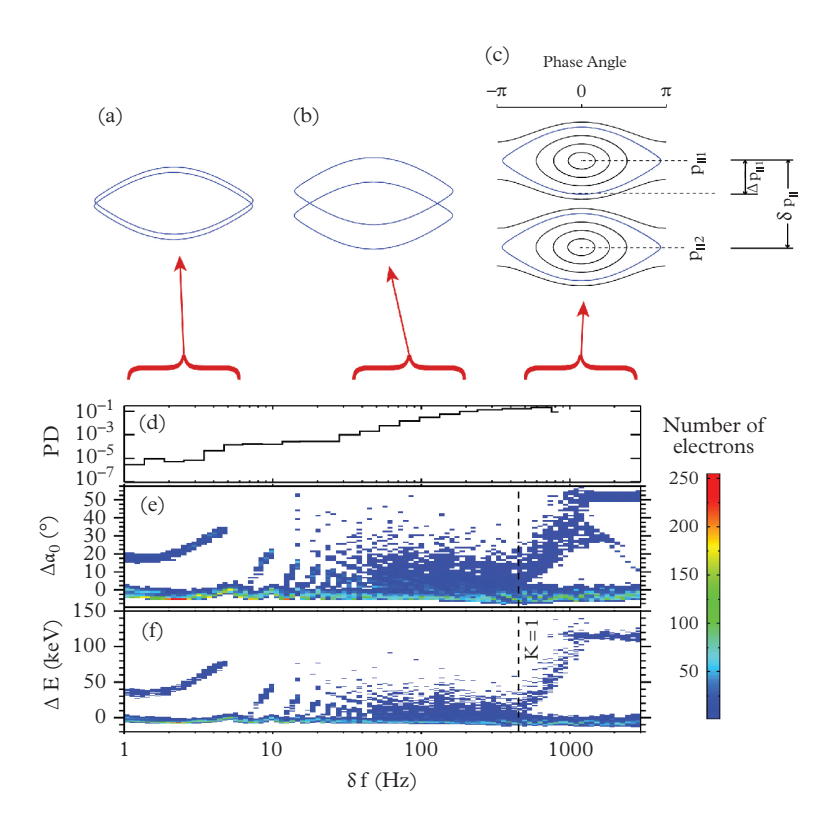


Figure 8.7 A two-wave model of the modulated wave amplitude, and particle scattering results. (a) The degenerate region, where waves have very closely spaced frequencies, (b) the stochastic region, where resonant islands overlap, and (c) the non-overlap region, where particles respond to each wave independently. (d) The distribution of subpacket frequency separations, (e) test particle scattering distributions as a function of frequency separation between the two component waves (f) similar to (e) but for particle energies.

These results suggest that the particle response in a typical chorus element will involve a complex interplay between the characteristic length of the subpacket structure (which controls $\delta p_{||}$), and the amplitude of the subpacket which controls the width of the resonant island and hence $\Delta p_{||}$. In general, we expect that nonlinear phase bunching and phase trapping effects will be somewhat reduced by the inclusion of subpacket structure. To demonstrate that this is the case, we show in Figure 8.8 the results of a simulation based on the work of Tao et al. [2012]. Here, a realistic chorus element, complete with frequency variation, subpacket structure, and amplitude modulation is modeled to accurately represent an observation of a chorus element made on THEMIS D on October 23, 2008, at L=6.4, near the geomagnetic equator. Figure 8.8a shows the observed chorus element and Figure 8.8b shows the modeled chorus element, both

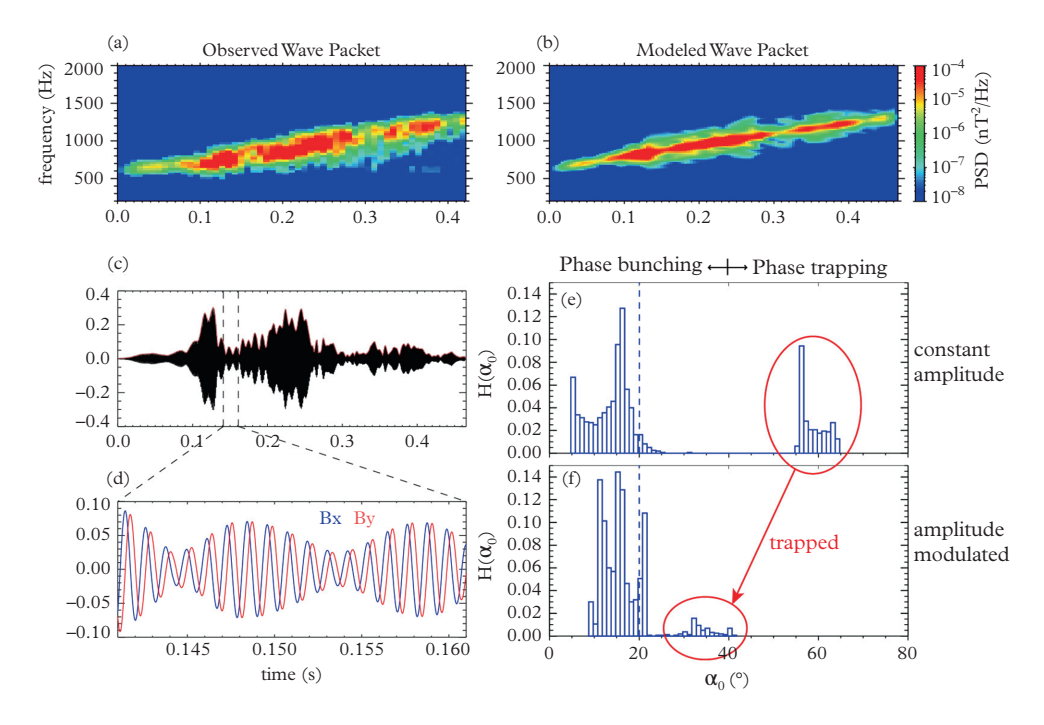


Figure 8.8 A realistic simulation of test particle scattering by an amplitude modulated chorus element. (a) An observed chorus element, and (b) the modeled chorus element representing the observation in panel (a), through which the test particles are propagated. (c) The amplitude of the Bx and By components of the chorus element for the duration of the element, and (d) an expanded view at a particular time, which is similar for both the observed and the simulated wave. (e) Test particle scattering in response to a constant amplitude wave and (f) in response to the amplitude modulated wave, showing that the trapped particles do not travel as far as in (e) but nevertheless still exhibit evidence of trapping effects.

having a time structure as shown in Figures 8.8c and 8.8d. A total of 1600 test particle electrons are run through the modeled wave packet, and a similar wave packet having constant amplitude and frequency to highlight the differences, as shown in Figures 8.8e and 8.8f. As expected, the population of particles that are trapped in the realistic wave packet (Figure 8.8f) has been substantially diminished compared to those in the constant amplitude wave, and the degree of scattering has been reduced, but qualitatively the test particle response still exhibits the signature of nonlinear scattering with a majority of particles advected to lower pitch angles and energies due to phase bunching, and a small fraction being advected to much larger pitch angles and energies due to phase trapping. The effect of multiple wave packets over an extended period of time on the test particles (e.g., Figure 8.4a) has not yet been determined but is the subject of current and ongoing research. Some early results suggest that the net effect is a very rapid acceleration of the tail of energetic electrons to high energies [Yoon, 2011].

8.5 Summary and conclusions

This chapter introduces and explores the resonant interaction between whistler mode chorus waves and energetic electrons, typical of the near-Earth space environment, and focuses specifically on those elements of the resonant interaction that are unique to chorus. As an example, Section 8.2 discussed the characteristics of chorus, and the unique structuring that it exhibits over a variety of spatial and temporal scales. Temporal structuring on the finest timescales, typically referred to as subelement structure, was shown in Section 8.4 to produce dynamics that are not typically captured in either the quasilinear diffusion framework or test particle simulations with a single wave of constant frequency and amplitude. These dynamics can be understood as a complex interplay of the chorus wave's characteristic intensity, compared to the typical periodicities of the chorus subelements. Test particle simulations with realistic wave packets show that while the classical nonlinear effects associated with constant, large-amplitude waves are reduced, the overall particle scattering is nevertheless far from linear, and global models of radiation belt variability will need to find novel ways of including the realistic particle scattering responses into the traditionally diffusion-based approaches.

In addition, many open questions remain about the physical processes that control the morphological features of chorus: the $\sim\!1$ Re spatial scale of magnetospheric chorus patches, and the associated $\sim\!$ minute timescales over which these patches pulsate, the $\sim\!1$ s timescale of the chorus elements themselves, what controls this timescale, the frequency drift, and separation between individual chorus elements. Finally, what is the physical process that controls the subelement structure within each chorus element, and how can it be modeled and understood. The unprecedented volume and quality of data currently being generated, including those data from the recently launched Van Allen Probes, together with the intense activity in this field at the moment, will undoubtedly answer many of these outstanding questions in the near future.

.....

REFERENCES

Agapitov, O., et al. (2013), Statistics of whistler-mode waves in the outer radiation belt: Cluster STAFF-SA measurements, J. Geophys. Res. Space Physics, 118, 3407–3420, doi:10.1002/jgra.50312.

Albert, J.M. (2000), Gyroresonant interactions of radiation belt particles with a monochromatic electromagnetic wave, J. Geophys. Res., 105 (A9), 21191–21209.

Albert, J. M. (2010), Diffusion by one wave and by many waves, J. Geophys. Res., 115, A00F05, doi:10.1029/2009JA014732.

Bortnik, J., U. S. Inan, and T. F. Bell (2006), Temporal signatures of radiation belt electron precipitation induced by lightning-generated MR whistler waves: 1. Methodology, *J. Geophys. Res.*, 111, A02204, doi:10.1029/2005JA011182.

Bortnik, J., and R. M. Thorne (2007), The dual role of ELF/VLF chorus waves in the acceleration and precipitation of radiation belt electrons, *J. Atmos. Solar Terr. Phys.*, **69**, 378–386.

- Bortnik, J., R. M. Thorne, and N. P. Meredith (2007), Modeling the propagation characteristics of chorus using CRRES suprathermal electron fluxes, J. Geophys. Res., 112, A08204, doi:10.1029/2006JA012237.
- Bortnik, J., Thorne, R.M., and Inan, U.S. (2008). Nonlinear interaction of energetic electrons with large amplitude chorus. *Geophys. Res. Lett.*, **35**, L21102, http://dx.doi.org/10.1029/2008GL035500.
- Burtis, W. J., and R. A. Helliwell (1969), Banded chorus—A new type of VLF radiation observed in the magnetosphere by OGO 1 and OGO 3, J. Geophys. Res., 74 (11), 3002–3010, doi:10.1029/JA074i011p03002.
- Cattell, C., et al. (2008), Discovery of very large amplitude whistler-mode waves in Earth's radiation belts. *Geophys. Res. Lett.*, **35**, L01105, http://dx.doi. org/10.1029/2007GL032009.
- Chen L., R. M. Thorne, W. Li, and J. Bortnik (2013), Modeling the wave normal distribution of chorus waves, J. Geophys. Res. Space Physics, 118, 1074–1088, doi:10.1029/2012JA018343.
- Cully, C.M., J.W. Bonnell, and R.E. Ergun (2008), THEMIS observations of long-lived regions of large-amplitude whistler waves in the inner magnetosphere. *Geophys. Res. Lett.*, 35, L17S16, http://dx.doi.org/10.1029/2008GL033643.
- Dysthe, K.B. (1971), Some studies of triggered whistler emissions, J. Geophys. Res. 76 (28), 6915–6931.
- Friedel, R. H. W., G. D. Reeves, and T. Obara (2002), Relativistic electron dynamics in the inner magnetosphere—A review, J. Atmos. Sol. Terr. Phys., 64, 265.
- Furuya, N., Y. Omura, and D. Summers (2008), Relativistic turning acceleration of radiation belt electrons by whistler mode chorus, J. Geophys. Res., 113, A04224, doi: 10.1029/2007JA012478.
- Helliwell, R. A. (1967), A theory of discrete emissions from the magnetosphere, J. Geophys. Res., 72, 4773–4790.
- Hikishima, M., Y. Omura, and D. Summers (2010), Microburst precipitation of energetic electrons associated with chorus wave generation, *Geophys. Res. Lett.*, 37, L07103, doi:10.1029/2010GL042678.
- Hikishima, M., and Y. Omura (2012), Particle simulations of whistler-mode rising-tone emissions triggered by waves with different amplitudes, *J. Geophys. Res.*, 117, A04226, doi: 10.1029/2011JA017428.
- Horne, R. B., and R. M. Thorne (2003), Relativistic electron acceleration and precipitation during resonant interactions with whistler-mode chorus, *Geophys. Res.*, *Lett.*, 30 (10), 1527, doi:10.1029/2003GL016973.
- Horne, R. B., R. M. Thorne, S. A. Glauert, J. M. Albert, N. P. Meridith, and R. R. Anderson (2005), Timescales for radiation belt electron acceleration by whistler mode chorus waves, J. Geophys. Res., 111, A03225, doi:10.1029/2004JA010811.
- Inan, U.S., T. F. Bell, and R. A. Helliwell (1978), Nonlinear pitch angle scattering of energetic electrons by coherent VLF waves in the magnetosphere, J. Geophys. Res., 83 (A7), 3235–3253.
- Isted, G. A., and G. Millington (1957), The "dawn chorus" in radio observations, *Nature*, **180**, 716.
- Katoh, Y., and Y. Omura (2006), A study of generation mechanism of VLF triggered emission by self-consistent particle code, J. Geophys. Res., 111, A12207, doi: 10.1029/2006JA011704.
- Katoh, Y., and Y. Omura (2007), Relativistic particle acceleration in the process of whistler-mode chorus wave generation, *Geophys. Res. Lett.*, **34**, L13102, doi: 10.1029/2007GL029758.
- Katoh, Y., and Y. Omura (2011), Amplitude dependence of frequency sweep rates of whistler mode chorus emissions, *J. Geophys. Res.*, **116**, A07201, doi: 10.1029/2011JA016496.
- Keika, K., M. Spasojevic, W. Li, J. Bortnik, Y. Miyoshi, and V. Angelopoulos (2012), PEN-GUIn/AGO and THEMIS conjugate observations of whistler mode chorus waves in the

- dayside uniform zone under steady solar wind and quiet geomagnetic conditions, J. Geophys. Res., 117 (A7), A07212.
- Kennel, C. F., and F. Engelman (1966), Velocity space diffusion from weak plasma turbulence in a magnetic field, *Phys. Fluids*, **9**, 2377.
- Kennel, C. F., and H. E. Petschek (1966), Limit on stably trapped particle fluxes, *J. Geophys. Res.*, 71 (1), 1–28, doi:10.1029/JZ071i001p00001.
- Lauben, D. S., U. S. Inan, T. F. Bell, D. L. Kirchner, G. B. Hospodarsky, and J. S. Pickett (1998), VLF chorus emissions observed by Polar during the January 10, 1997, magnetic cloud, Geophys. Res. Lett., 25 (15), 2995–2998.
- Lauben, D. S., U. S. Inan, T. F. Bell, and D. A. Gurnett (2002), Source characteristics of ELF/VLF chorus, J. Geophys. Res., 107 (A12), 1429, doi:10.1029/2000JA003019.
- LeDocq, M. J., D. A. Gurnett, and G. B. Hospodarsky (1998), Chorus source locations from VLF Poynting flux measurements with the Polar spacecraft, *Geophys. Res. Lett.*, **25** (21), 4063–4066.
- Lichtenberg, A., and M. Lieberman (1983), *Regular and Chaotic Dynamics*, second ed. Springer Verlag, New York.
- Li, W., et al. (2009), Evaluation of whistler-mode chorus intensification on the nightside during an injection event observed on the THEMIS spacecraft, J. Geophys. Res., 114, A00C14, doi:1029/2008JA013554.
- Li, W., et al. (2010), THEMIS analysis of observed equatorial electron distributions responsible for the chorus excitation, *J. Geophys. Res.*, 115, A00F11, doi: 10.1029/2009JA014845.
- Li, W., J. Bortnik, Y. Nishsimura, R. M. Thorne, and V. Angelopoulos (2012), The origin of pulsating aurora: modulated whistler mode chorus waves, in *Auroral Phenomenology and Magnetospheric Processes: Earth and Other Planets, Geophysical Monograph Series* 197, AGU, 10.1029/2011GM001164.
- Li, W., J. Bortnik, R. M. Thorne, Y. Nishimura, V. Angelopoulos, and L. Chen (2011), Modulation of whistler mode chorus waves: 2. Role of density variations, J. Geophys. Res., 116, A06206, doi:10.1029/2010JA016313.
- Li, W., et al. (2013a), Characteristics of the Poynting flux and wave normal vectors of whistler-mode waves observed on THEMIS, J. Geophys. Res. Space Physics, 118, 1461–1471, doi: 10.1002/jgra.50176.
- Li, W., et al. (2013b), Constructing the global distribution of chorus wave intensity using measurements of electrons by the POES satellites and waves by the Van Allen Probes, *Geophys. Res. Lett.*, 40, 4526–4532, doi: 10.1002/grl.50920.
- Mauk, B. H., et al. (2012), Science objectives and rationale for the radiation belt storm probes mission, *Space Sci. Rev.*, 1–15, doi:10.1007/s11214-012-9908-y.
- Meredith, N. P., R. B. Horne, R. M. Thorne, and R. R. Anderson (2003), Favored regions for chorus-driven electron acceleration to relativistic energies in the Earth's outer radiation belt, *Geophys. Res. Lett.*, 30, 1871, doi:10.1029/2003GL017698, 16.
- Meredith, N. P., et al. (2012), Global model of lower band and upper band chorus from multiple satellite observations, J. Geophys. Res., 117, A10225.
- Ni, B., R. M. Thorne, N. P. Meredith, R. B. Horne, and Y. Shprits (2011), Resonant scattering of plasma sheet electrons leading to diffuse auroral precipitation: 2. Evaluation for whistler-mode chorus waves, *J. Geophys. Res.*, **116**, A04219, doi:10.1029/2010JA016233.
- Nishimura, Y., et al. (2010), Identifying the driver of pulsating aurora, *Science*, 330, 81–84, doi:10.1126/science.1193186.
- Nishimura, Y, et al. (2011), Multi-event study of the correlation between pulsating aurora and whistler-mode chorus emissions, J. Geophys. Res., 116, A11221, doi:10.1029/2011JA016876.
- Nunn, D. (1974), A self-consistent theory of triggered VLF emissions, Planet. Space Sci., 22, 349.

- Nunn, D., Y. Omura, H. Matsumoto, I. Nagano, and S. Yagitani (1997), The numerical simulation of VLF chorus and discrete emissions observed on the Geotail satellite using a Vlasov code, *J. Geophys. Res.*, **102** (A12), 27,083–27,098, doi:10.1029/97JA02518.
- Omura, Y., N. Furuya, and D. Summers (2007), Relativistic turning acceleration of resonant electrons by coherent whistler mode waves in a dipole magnetic field. *J. Geophys. Res.*, 112, A06236, http://dx.doi.org/10.1029/2006JA012243.
- Omura, Y., Y. Katoh, and D. Summers (2008), Theory and simulation of the generation of whistler-mode chorus, J. Geophys. Res., 113, A04223, doi: 10.1029/2007JA012622.
- Omura, Y., M. Hikishima, Y. Katoh, D. Summers, and S. Yagitani (2009), Nonlinear mechanisms of lower-band and upper-band VLF chorus emissions in the magnetosphere, *J. Geophys. Res.*, 114, A07217, doi: 10.1029/2009JA014206.
- Omura, Y., and D. Nunn (2011), Triggering process of whistler mode chorus emissions in the magnetosphere, J. Geophys. Res., 116, A05205, doi:10.1029/2010JA016280.
- Roederer, J. G. (1970), Dynamics of Geomagnetically Trapped Radiation, Springer, New York.
- Santolík, O., and D. A. Gurnett (2003), Transverse dimensions of chorus in the source region, *Geophys. Res. Lett.*, **30** (2), 1031, doi:10.1029/2002GL016178.
- Santolík, O., D. A. Gurnett, J. S. Pickett, M. Parrot, and N. Cornilleau-Wehrlin (2004), A microscopic and nanoscopic view of storm-time chorus on 31 March 2001, Geophys. Res. Lett., 31, L02801, http://dx.doi.org/10.1029/2003GL018757.
- Santolík, O., J. S. Pickett, D. A. Gurnett, J. D. Menietti, B. T. Tsurutani, and O. Verkhogly-adova (2010), Survey of Poynting flux of whistler mode chorus in the outer zone, *J. Geophys. Res.*, 115, A00F13, doi: 10.1029/2009JA014925.
- Santolík, O., E. Macúšová, I. Kolmašová, N. Cornilleau-Wehrlin, and Y. de Conchy (2014), Propagation of lower-band whistler-mode waves in the outer Van Allen belt: Systematic analysis of 11 years of multi-component data from the Cluster spacecraft, *Geophys. Res. Lett.*, 41, 2729–2737, doi:10.1002/2014GL059815.
- Shklyar, D., and H. Matsumoto (2009), Oblique whistler mode waves in the inhomogeneous magnetospheric plasma: resonant interactions with energetic charges particles, *Surv. Geophys.*, **30**, 55–104, doi: 10.1007/s10712-009-9061-7.
- Storey, L. R. O. (1953), An investigation of whistling atmospherics, *Phil. Trans. Roy. Soc. London*, A246, 113–141.
- Summers, D., R. M. Thorne, and F. Xiao (1998), Relativistic theory of wave-particle resonant diffusion with application to electron acceleration in the magnetosphere, *J. Geophys. Res.*, **103**, 20,487–20,500.
- Summers, D., et al. (2002), Model of the energization of outer-zone electrons by whistler-mode chorus during the October 9, 1990 geomagnetic storm, *Geophys. Res. Lett.*, 29 (24), 2174, doi:10.1029/2001GL016039.
- Tao, X., J. Bortnik, J. M. Albert, K. Liu, and R. M. Thorne (2011b), Comparison of quasilinear diffusion coefficients for parallel propagating whistler mode waves with test particle simulations, *Geophys. Res. Lett.*, 38, L06105, doi:10.1029/2011GL046787.
- Tao, X., R. M. Thorne, W. Li, B. Ni, N. P. Meredith, and R. B. Horne (2011a), Evolution of electron pitch-angle distributions following injection from the plasma sheet, J. Geophys. Res., 116, A04229, doi:10.1029/2010JA016245.
- Tao, X., J. Bortnik, J. M. Albert, and R. M. Thorne (2012), Comparison of bounce-averaged quasi-linear diffusion coefficients for parallel propagating whistler mode waves with test particle simulations, J. Geophys. Res., 117, A10205, doi:10.1029/2012JA017931.
- Tao, X., J. Bortnik, J. M. Albert, R. M. Thorne, and W. Li (2013), The importance of amplitude modulation in nonlinear interactions between electrons and large amplitude whistler waves, J. Atmos. Sol.-Terr. Phys., 99, 67–72.

- Thorne, R. M. (2010), Radiation belt dynamics: The importance of wave-particle interactions, *Geophys. Res. Lett.*, 37, L22107, doi:10.1029/2010GL044990.
- Thorne, R. M., B. Ni, X. Tao, R. B. Horne, and N. P. Meredith (2010), Scattering by chorus waves as the dominant cause of diffuse auroral precipitation, *Nature*, **467**, 943–946, doi:10.1038/nature09467.
- Thorne, R. M., et al. (2013), Rapid local acceleration of relativistic radiation belt electrons by magnetospheric chorus, *Nature*, Paper #2013-08-11553B.
- Trakhtengerts, V.Y. (1999), A generation mechanism for chorus emissions. *Ann. Geophys.*,17, 95–100.
- Tsurutani, B. T., and E. J. Smith (1974), Postmidnight chorus: A substorm phenomenon, *J. Geophys. Res.*, 79 (1), 118–127, doi:10.1029/JA079i001p00118.
- Tsurutani, B. T., and E. J. Smith (1977), Two types of magnetospheric ELF chorus and their substorm dependencies, J. Geophys. Res., 82 (32), 5112–5128, doi:10.1029/JA082i032p05112.
- Turner, D. L., V. Angelopoulos, Y. Shprits, A. Kellerman, P. Cruce, and D. Larson (2012), Radial distributions of equatorial phase space density for outer radiation belt electrons, *Geophys. Res. Lett.*, 39, L09101, doi: 10.1029/2012GL051722.
- Walt, M. (1994), *Introduction to geomagnetically trapped radiation*, Cambridge University Press, Cambridge.
- Walker, A. D. M. (1993), Plasma waves in the magnetosphere, Springer-Verlag, New York, 1993.
- Yoon, P.H. (2011), Large-amplitude whistler waves and electron acceleration. *Geophys. Res. Lett.*, 38, L12105, http://dx.doi.org/10.1029/2011GL047893.
- Zaslavsky, G.M. (1985), Chaos in Dynamic Systems, Harwood Academic Publishers, New York.